Journal of Physics D: Applied Physics

PAPER • **OPEN ACCESS**

Reconfigurable THz leaky-wave antennas based on innovative metal–graphene metasurfaces

To cite this article: Edoardo Negri *et al* 2024 *J. Phys. D: Appl. Phys.* **57** 485102

OPEN ACCESS
IOP Publishing
Journal of Physics D: Applied Physics
J. Phys. D: Appl. Phys. **57** (2024) 485102 (9pp)
https://doi.org/10.1088/1361-6463/ad7302

Reconfigurable THz leaky-wave antennas based on innovative metal–graphene metasurfaces

Edoardo Negri[1,*], **Walter Fuscaldo**[2,*], **Paolo Burghignoli**[1] and **Alessandro Galli**[1]

[1] Department of Information Engineering, Electronics and Telecommunications, Sapienza University of Rome, Rome 00184, Italy
[2] Istituto per la Microelettronica e i Microsistemi, Consiglio Nazionale delle Ricerche, Rome 00133, Italy

E-mail: edoardo.negri@uniroma1.it and walter.fuscaldo@cnr.it

Received 20 April 2024, revised 30 July 2024
Accepted for publication 23 August 2024
Published 5 September 2024

Abstract

Graphene ohmic losses notably hinder the efficiency of graphene-based terahertz (THz) devices. Hybrid metal–graphene structures have recently been proposed to mitigate this issue in a few passive devices, namely waveguide and Vivaldi antennas, as well as frequency selective surfaces. In this work, such a technique is extensively investigated to optimize the radiation performance of a THz Fabry–Perot cavity leaky-wave antenna based on a hybrid metal–graphene metasurface consisting of a lattice of square *metallic* patches interleaved with a complementary *graphene* strip grating. Theoretical, numerical, and full-wave results demonstrate that, by properly selecting the unit-cell features, a satisfactory trade-off among range of reconfigurability, antenna directivity, and losses can be achieved. The proposed antenna can find application in future wireless THz communications.

Keywords: reconfigurable antennas, leaky-wave antennas, metasurfaces, graphene, THz frequencies

1. Introduction

The possibility to design reconfigurable, planar, directive, and efficient antennas in the terahertz (THz) range has widely been investigated in the recent years [1] due to the increasing interest in many practical THz applications, such as high-resolution imaging [2], security screening [3], and wireless communications [4].

Thanks mainly to its tunable properties, graphene has extensively been promoted as a privileged platform for tunable THz antennas on a theoretical basis [5–8]. Among the possible THz reconfigurable radiating devices, Fabry–Perot cavity leaky-wave antennas (FPC-LWAs) have widely attracted attention thanks to their low-profile and high-directivity features [9, 10]. In the THz range, reconfigurability in FPC-LWAs can be achieved, for instance, by alternating layers of low-loss dielectric and highly birefringent nematic liquid crystals [11] or uniform as well as patterned graphene sheets [12, 13]. However, the design of graphene FPC-LWAs was based on a rather optimistic assumption on the quality of the graphene flake. It was later recognized [14] that the non-negligible ohmic losses, exhibited by commercially available graphene [15, 16], may hinder the realization of efficient THz antennas—and in particular FPC-LWAs [17]— based on graphene.

Recently, hybrid metal–graphene configurations have been proposed in order to reduce losses and achieve reconfigurability features with respect to fully graphene or fully metal structures, respectively. The simultaneous usage of these two materials has been investigated for the implementation of multiband THz frequency-selective surfaces

* Authors to whom any correspondence should be addressed.

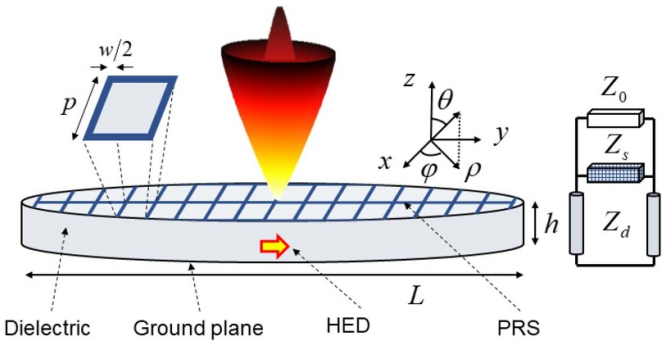

Figure 1. Pictorial representation of an FPC-LWA and its far-field radiation pattern (scanning conical and broadside pencil beams). The device is constituted by a grounded dielectric slab with a PRS on top and it is excited by a horizontal electric dipole (HED) on the ground plane. On the top-left corner, a zoomed representation of the innovative unit cell proposed in this work is shown: a graphene square frame (in blue) surrounding a metallic patch (in grey). On the right, the transverse equivalent network of the device is reported. Z_0 and Z_d are the characteristic impedances of the transmission-line model in air and in the substrate, and Z_s is the equivalent surface impedance of the PRS.

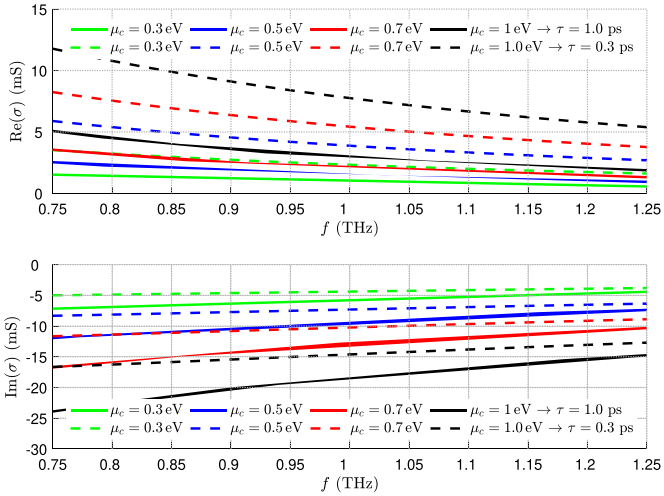

Figure 2. Real and imaginary part of the graphene surface conductivity σ vs. frequency f for different chemical potentials μ_c (different labeled colors) and for both a quasi-ideal and a realistic model of the material with $\tau = 1.0$ ps (solid lines) and $\tau = 0.3$ ps (dashed lines), respectively.

(FSS) [18], waveguide antennas [19], and Vivaldi antennas [20]. However, no attempts have been made for FPC-LWAs. Moreover, none of the previous works analyzes the trade-off among efficiency, directivity, and range of reconfigurability that typically affects antennas based on tunable materials (see, e.g. [21]).

In this paper, the idea of using hybrid metal–graphene metasurfaces is exploited for proposing a more realistic, reconfigurable, directive, THz FPC-LWA. The unit cell of the proposed metasurface is constituted by a subwavelength square metallic patch surrounded by a graphene strip grating, as shown in figure 1. Design criteria are provided to properly select the graphene and metal filling factors, in order to deal with the reconfigurabiliy vs. efficiency trade-off.

An optimal theoretical design, with an innovative simple formula for the directivity evaluation, is then obtained and corroborated by full-wave simulations on CST Microwave Studio [22], showing a remarkable agreement. Results demonstrate that the proposed antenna can be a promising candidate for future tunable, directive, planar THz radiating devices.

The paper is organized as follows. In section 2, the theoretical aspects related to the graphene features and the leaky-wave approach are shortly reported. In section 3, the features of the innovative metasurface unit cell are discussed. In section 4, the radiating performance of the proposed reconfigurable antenna architecture is analyzed. Conclusions are finally drawn in section 5.

2. Theoretical approach

In this section, the theoretical aspects related to the description of the graphene features and to the leaky-wave approach are briefly reported.

2.1. Graphene features

Graphene is a two-dimensional (2D) material, whose surface conductivity σ in the low THz range and room temperature ($T \simeq 300$ K) has a Drude-like behavior, as described by the intraband contributions of the Kubo formula (1) [23] (a time-harmonic dependence $\exp(j\omega t)$ is assumed throughout the paper):

$$\sigma = \frac{\tau q_e^2 k_B T}{\pi \hbar^2 (1 + j\omega\tau)} \left[\frac{\mu_c}{k_B T} + 2\ln\left(e^{-\frac{\mu_c}{k_B T}} + 1\right) \right] \qquad (1)$$

being q_e and $\hbar$ the electron charge and the reduced Planck constant, respectively, $\omega = 2\pi f$ the angular frequency (f being the frequency), and k_B the Boltzmann constant. The most important parameters are the relaxation time τ and the chemical potential μ_c, which both depend on the synthesis process of the graphene (usually chemical vapor deposition, CVD) and its quality [24]. The former is here set to $\tau = 1$ ps and $\tau = 0.3$ ps, which are a quasi-ideal and a realistic value for CVD-grown graphene samples, respectively [14], whereas the latter is allowed to vary from 0 eV to 1 eV, a range which is compatible with suitable biasing schemes (see, e.g. [25] for details). In particular, a single-layer graphene sheet is exploited in this work. The latter is totally described by the surface conductivity σ reported in figure 2 and computed by (1) by assuming a *quasi-ideal* ($\tau = 1$ ps) and a *realistic* ($\tau = 0.3$ ps) model of the graphene with $\mu_c = 0.3, 0.5, 0.7$, and 1.0 eV. It is worth pointing out that a recent experimental validation of the considered graphene properties has been addressed through time-domain spectroscopy in reflection mode on metal-backed dielectric substrates in [16].

2.2. The leaky-wave approach

A grounded dielectric slab covered with a partially reflecting sheet (PRS) is an example of FPC-LWA (see figure 1). Radiation from FPC-LWAs can conveniently be described by means of leaky-wave theory [26]. As shown in [17], a horizontal electric dipole (HED) or a horizontal magnetic dipole (HMD) source, typically realized by etching a quasi-resonant rectangular slot on the ground plane [27], excites a pair of transverse electric (TE) and transverse magnetic (TM) *leaky* modes [28, 29]. These modes represent the dominant contribution to radiation [30] and their main features strongly depend on the values of the complex *leaky*, radial wavenumber $k_\rho = \beta - j\alpha$.

While the leaky-wave phase constant β mainly affects the LWA pointing angle, the attenuation (or *leakage*) constant α accounts for all loss mechanisms in the structure, namely dielectric losses in the substrate α_{sub}, ohmic losses in the PRS α_{PRS}, and the desired radiation loss α_{rad} [31]. If there is just a single, dominant leaky-mode pair, the radiation efficiency η_r [31] can be accurately evaluated with the following two equations:

$$\alpha = \sqrt{\alpha_{\text{rad}}^2 + \alpha_{\text{PRS}}^2 + \alpha_{\text{sub}}^2} \tag{2}$$

$$\eta_r = (\alpha_{\text{rad}}/\alpha)^2 \tag{3}$$

where α_{rad} can be taken as the average between the attenuation constants of the TE and TM leaky wavenumbers. The total efficiency η_{tot} (assuming negligible insertion losses) is given by the radiation efficiency η_r multiplied by the aperture efficiency $\eta_{\text{ap}} = 1 - e^{-2\alpha L}$ [26], being L the radiating aperture size [31]:

$$\eta_{\text{tot}} = \eta_{\text{ap}} \cdot \eta_r. \tag{4}$$

The leakage constants of the dominant TE and TM leaky modes also mainly determine the beamwidth of the radiated beam. For pencil beams at broadside ($\beta \simeq \alpha$), the beamwidths are approximately the same in all elevation planes and given by [28]:

$$\Delta\theta = 2\sqrt{2}\hat{\alpha}^{\text{TM, TE}} \tag{5}$$

whereas for scanned beams (when $\beta \gg \alpha$), the beamwidths along the principal H- and E-planes are given by:

$$\Delta\theta_{\text{E,H}} = 2\hat{\alpha}^{\text{TM,TE}} \sec\theta_{\text{p}}^{\text{TM, TE}}. \tag{6}$$

The value θ_{p} represents the pointing angle (measured from the vertical z-axis), which is strictly related to the leaky phase constant β through the equation (7):

$$\sin\theta_{\text{p}} = \sqrt{\hat{\beta}^2 - \hat{\alpha}^2}, \tag{7}$$

where the 'hat' $\hat{(\cdot)}$ refers to quantities normalized with respect to the free-space wavenumber k_0, i.e. $\hat{\beta} = \beta/k_0$ and $\hat{\alpha} = \alpha/k_0$.

As is known, FPC-LWAs typically exhibit a frequency-scanning behavior due to the frequency-dependent character of any complex leaky wavenumber, whose variation with frequency (the dispersion diagram) can be retrieved from a straightforward application of the transverse resonance technique (TRT) [32] to the transverse equivalent network (TEN) of the device (see figure 1).

The dispersion curves of an FPC-LWA and, in turn, its radiating features, are mainly affected by the cavity height h, the dielectric filling, and the PRS. The latter is here described by a single scalar sheet impedance $Z_s = R_s + jX_s$ (the validity of this assumption is demonstrated in the next section 3) [33]. The cavity height h is commonly set to maximize the radiated power at broadside [34, 35] through the formula

$$h \simeq \frac{\lambda}{2\sqrt{\varepsilon_r}}\left(1 - \frac{X_s}{\pi\eta_0}\right) \tag{8}$$

being λ the wavelength at the desired working frequency, η_0 the free-space impedance, and ε_r and $\tan\delta$ the relative permittivity and the loss tangent of the FPC-LWA dielectric filling, respectively. The latter are here set to $\varepsilon_r = 2.3$ and $\tan\delta \simeq 0.001$, which corresponds to the values exhibited by Zeonor at THz frequencies [36].

The FPC-LWA directivity D_0 can be theoretically predicted by exploiting different formulas depending on the radiation conditions. Assuming an infinitely extended radiating aperture and considering the average among TE and TM components for $\hat{\alpha}$, D_0 is given by the typical formula (9) for broadside pencil beams [17]:

$$D_0 \simeq \pi^2/\left(8\hat{\alpha}^2\right). \tag{9}$$

However, in the case of scanned conical beams, there is not a simple expression in the available literature for the antenna directivity (at the best of the Authors' knowledge). For this reason, starting from the directivity definition [37] and by considering the theoretical radiation patterns of LWAs [28], we analytically estimated D_0 for small beamwidth values as:

$$D_0 \simeq \cot\theta_{\text{p}}/\hat{\alpha}. \tag{10}$$

Equation (10) approximately holds only for small beamwidth values, which is, nevertheless, the typical and desired working condition for FPC-LWA. The validity and limitations of this assumption are corroborated by a comparison among full-wave and analytical results in section 4.

3. Innovative metal–graphene unit cells

An innovative hybrid metal–graphene unit cell for THz FPC-LWAs is here proposed as a viable means to introduce reconfigurability in a metasurface with a minimal impact on the ohmic losses and in turn on the overall antenna efficiency. On one hand, typical metal-only metasurfaces in the THz range are realized by patterning a good metal (almost lossless) over a low-loss polymer through photolitographic processes [38]. These metasurfaces in FPC-LWAs are able to generate a directive radiation pattern with negligible losses in the THz frequency range [38]. However, simple metallic structures are not able to reconfigure the radiating properties of

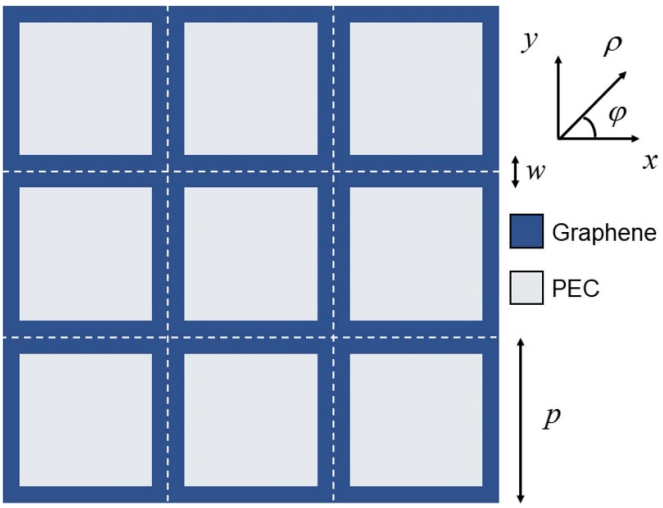

Figure 3. Top view of a portion of the proposed hybrid metal–graphene PRS with the representation of the unit-cell design parameters.

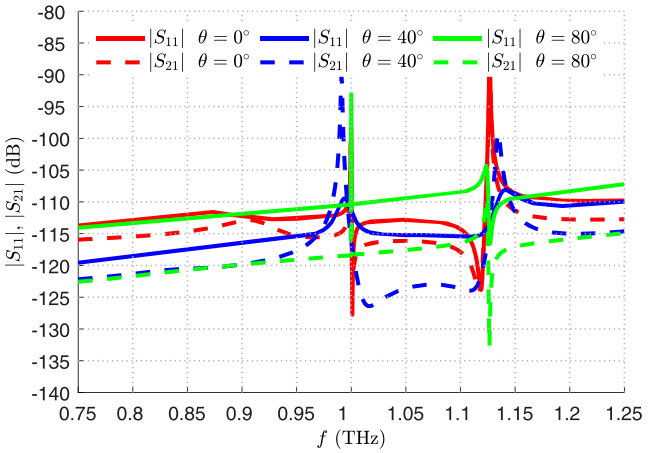

Figure 4. Reflection $|S_{11}|$ (solid lines) and transmission $|S_{21}|$ (dashed lines) coefficient of generated TE Floquet waves when the effect of an incident TM Floquet wave on a metal–graphene PRS unit cell is considered with different angles of incidence θ. The unit-cell configuration considered for this simulation is the case with $p = \lambda_0/5$, $w = 0.1p$, $\tau = 1$ ps, and $\mu_c = 0.3$ eV.

the device. On the other hand, graphene-only THz metasurfaces are typically realized by growing mono-layer or few-layer graphene through CVD on copper foils and then transferring it over a low-loss polymer where it can possibly be patterned. Such metasurfaces feature reconfigurable properties, provided graphene is suitably biased through the application of a DC voltage between the graphene layer itself and a thin weakly conductive film placed few tens of nanometers beneath. However, they show non-negligible losses due to the relatively large value of sheet resistance (several hundreds of Ω/sq) exhibited by graphene in the THz range [16]. It is worthwhile to point out that a fair comparison among FPC-LWAs based on fully graphene and the proposed metal–graphene unit cells is not an easy task. Previous works based on graphene-only metasurfaces have indeed taken into account the graphene losses, but with an ideal model of the material [25]. It is however clear that, with fully graphene metasurfaces, a higher reconfigurability is achieved at the expense of lower efficiencies with respect to hybrid metal–graphene unit cells.

Therefore, the implementation of a hybrid metal–graphene configuration allows us to maintain the reconfigurable properties of the device while maintaining acceptable losses. For this purpose, as shown in figure 3, the proposed unit cell with period $p = \lambda_0/5$ (being λ_0 the vacuum wavelength at $f_0 = 1$ THz) is constituted by a graphene strip grating, with width w, surrounding an ideal perfect-electric-conductor patch (since good metals as aluminum are almost lossless in this frequency range [38]).

First, it is verified that such metasurface can be fully described by a scalar sheet impedance Z_s by showing that the off-diagonal components of the dyadic sheet impedance are negligible. For this purpose, we analyzed the generalized scattering properties of the unit cell (for the sake of brevity, only the case of a quasi-ideal graphene strip with width $w = 0.1p$ and $\mu_c = 0.3$ eV is shown) looking at the reflected (through S_{11}) or transmitted (through S_{21}) TE-polarized Floquet waves under the excitation of a TM Floquet wave at different angles θ and $\phi = 45°$. Results are shown in figure 4, where it is seen that the cross-coupling effect is always negligible since any TE-polarized contribution generated by an incident TM Floquet wave is -80 dB with respect to the incoming wave. This aspect has been verified for numerous combinations of polarization incidence, relaxation time, graphene portion, and chemical potential obtaining similar results.

Once it has been verified that the metasurface does not show cross-coupling effects and has almost the same impedance behavior for TM and TE polarizations (as verified later in this section), the PRS can be represented by a scalar impedance sheet $Z_s = R_s + jX_s$ and, thus, it is possible to simply choose its design parameters. The rationale behind the design of such unit cell is to achieve a good reconfigurability (the reactance X_s value can significantly change as the tuning parameter μ_c is varied through a biasing voltage), while maintaining acceptable ohmic losses.

The sheet impedance Z_s is evaluated from full-wave simulations (CST Microwave Studio [22]) of the unit-cell scattering parameters, as previously discussed in [38]. In figure 5, these results are reported for both a quasi-ideal and a realistic graphene, modeled with $\tau = 1$ ps and $\tau = 0.3$ ps, respectively, and considering a normal incidence on the metasurface for different unit-cell configurations (different strip widths w/p of graphene) and chemical potential values μ_c. For the case of a quasi-ideal graphene ($\tau = 1$ ps), an excellent reconfigurable property can be achieved since losses (related to the R_s value) are acceptable for any graphene filling factor and a large X_s variation can be obtained. (A large variation of X_s determines a large variation of the pointing angle.) In the case of a realistic graphene ($\tau = 0.3$ ps), although a large variation of X_s (and hence a good degree of reconfigurability) can be obtained for any graphene filling factor, we achieve acceptable losses only for rather small graphene strips (relatively low R_s values).

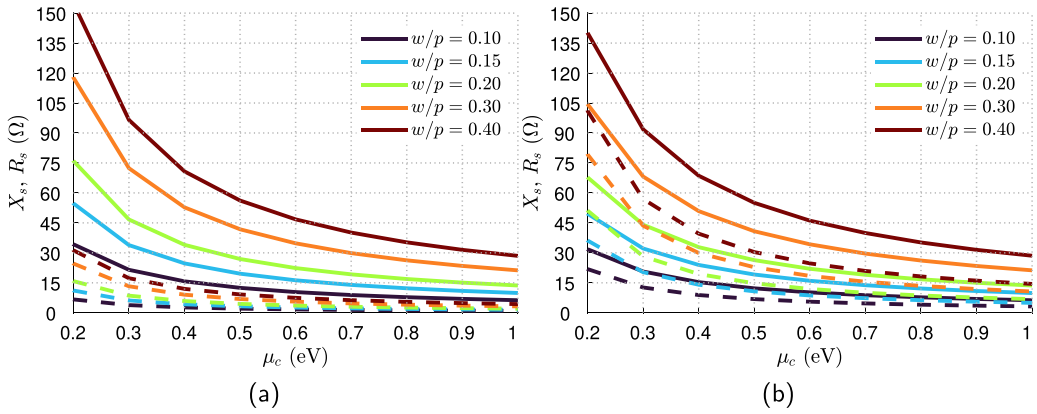

Figure 5. Equivalent reactance X_s (solid lines) and resistance R_s (dashed lines) at $f_0 = 1$ THz for different graphene-strip width w vs. chemical potential μ_c when a normal incidence is considered on the metasurface with periodicity $p = \lambda_0/5$. The model of the graphene considers a relaxation time (a) $\tau = 1$ ps and (b) $\tau = 0.3$ ps.

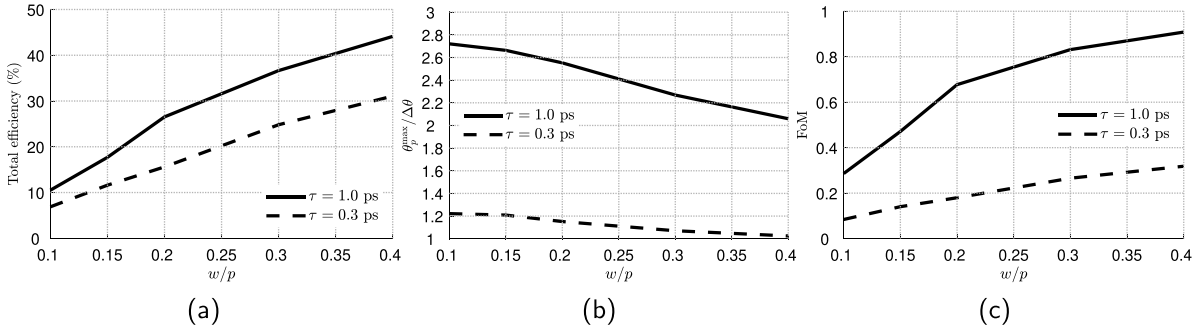

Figure 6. Plot of (a) the total radiation efficiency, (b) reconfigurability level (given by the maximum reachable pointing angle normalized with respect to the average beamwidth), and (c) figure of merit as a product of the efficiency and reconfigurability vs. the graphene filling factor w/p. The analyses consider a normal incidence at $f_0 = 1$ GHz on the unit cell with both a realistic (dashed lines: $\tau = 0.3$ ps) and quasi-ideal (solid lines: $\tau = 1$ ps) graphene model.

In order to provide a design rule for the graphene filling factor, i.e. the width of the graphene strip in the unit-cell configuration, a figure of merit (FoM) has been defined in this work. The latter, similar to the one discussed in [21], is given by the product of the total efficiency η_{tot} (computed assuming an aperture size of the antenna L sufficiently high so that $\eta_{\text{ap}} \to 1$) and a sort of *effective* tunable range, i.e. the tunable maximum pointing angle $\theta_p^{\max}$ (achieved for $\mu_c = 0.3$ ps, as discussed in detail in section 4) normalized to the half-power beamwidth $\Delta\theta$. In formulas:

$$\text{FoM} = \eta_{\text{tot}} \frac{\theta_p^{\max}}{\Delta\theta}. \tag{11}$$

It is worthwhile to point out that, for each graphene-width value and for both the case of a quasi-ideal ($\tau = 1$ ps) and realistic ($\tau = 0.3$ ps) model, both the total efficiency and the beamwidth for the FoM are averaged with respect to the range of values obtained for $0.3\ \text{eV} \leqslant \mu_c \leqslant 1\ \text{eV}$.

Results of the design process are reported in figure 6. As expected, the efficiency, the tunable range, and, in turn, the FoM increase when a quasi-ideal graphene ($\tau = 1$ ps) is assumed rather than a realistic graphene representation ($\tau = 0.3$ ps). Interestingly, as the portion of the graphene increases, the total efficiency of the device increases but its normalized tunable range decreases. Although it may appear counterintuitive (a larger portion of graphene translates into higher ohmic losses), this behavior agrees with the theoretical expectation as a result of two effects. First, as shown in figure 5, as w/p increases, both R_s and X_s increase, but the latter increase at a higher rate. Second, for $R_s \ll X_s$ (a condition satisfied by these unit cells), radiation losses scale linearly with X_s while PRS losses scale linearly with $\sqrt{R_s}$ [31]. Therefore, for large w/p values the antenna is expected to show a higher radiation efficiency (as confirmed by the trend of figure 6(a)) at the expense of a less directive behavior (due to the higher radiation losses). As per the definition of the FoM in (11), one should prefer a hybrid metal–graphene unit cell with a large graphene portion, at the expense of a lower directivity (see figure 6).

However, since in this work the idea is to achieve a good reconfigurability property (high $\theta_p^{\max}$ values with small beamwidths), the graphene strip width is hereafter fixed at $w = 0.1p$. Larger metallic filling factors correspond indeed to lower X_s values (a zero value is consistently achieved in the asymptotic limit of an all-metal lossless metasurface) and, in turn, to higher directivity [17]. It is worthwhile to point out that different design choices can obviously be taken depending on the targeted application and the related desired antenna features.

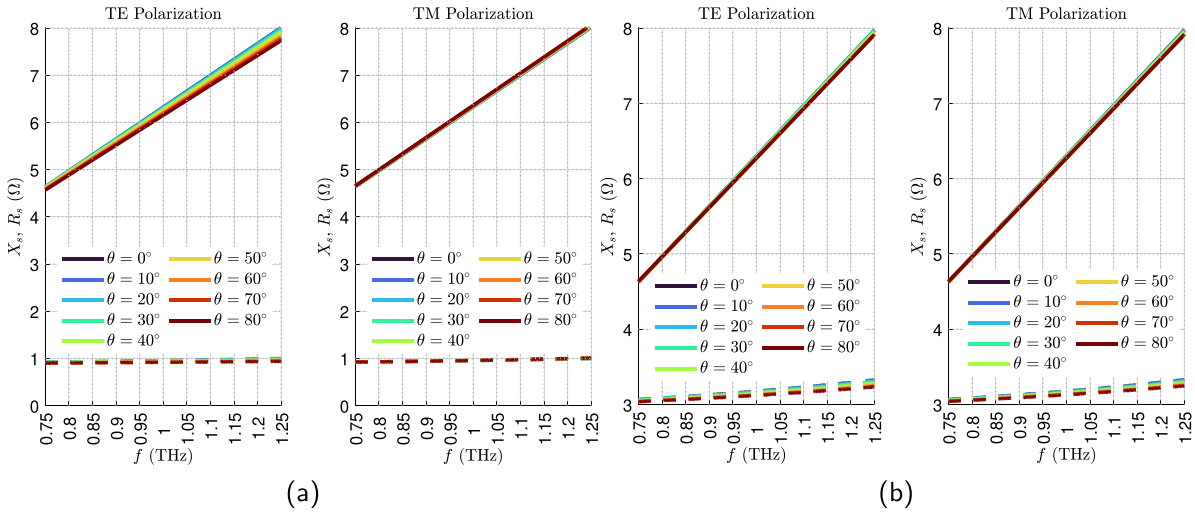

Figure 7. Equivalent reactance X_s (solid lines) and resistance R_s (dashed lines) for different Floquet-wave incident angles θ vs. frequency f when a PRS unit cell with $p = \lambda_0/5$, $w = 0.1p$, and (a) $\tau = 1$ ps or (b) $\tau = 0.3$ ps is considered.

It is worth pointing out that normal incidence has been considered so far and, therefore, the equivalent PRS impedance acts the same for both TE and TM polarizations. However, the idea is to implement a reconfigurable FPC-LWA which works at different pointing angles. Fortunately, as shown in figure 7, for both the graphene models, the proposed hybrid metal–graphene unit cell shows a negligible spatial dispersion and almost the same behavior for each polarization. This property is of crucial importance because it allows for considering Z_s as a function of the frequency f only, without including the wavenumber dependence [38].

Since a reconfigurable, planar, low-loss, spatial-dispersion- and cross-coupling-free metasurface has been achieved with the proposed innovative hybrid metal–graphene configuration, it has been used for the implementation of a directive, and low-profile FPC-LWA in the THz frequency range whose parameters are discussed in the following section 4. In particular, the unit cell with the graphene-strip width $w = 0.1p$ has been considered with $\mu_c = 0.3, 0.5, 0.7, 1.0$ eV in the case of a $\tau = 1$ ps and $\tau = 0.3$ ps graphene model, obtaining the equivalent surface impedance reported in figure 8.

4. Radiation performance

The performance of FPC-LWAs based on a hybrid metal-graphene metasurface with $w/p = 0.1$ (the high-directive case study described in section 3) is analyzed here in terms of radiation pattern, directivity, and pointing angle through the leaky-wave approach. Results are corroborated through frequency-domain full-wave simulations of a finite-size structure excited by an ideal HED along the y-axis (see figure 1) [22].

The FPC-LWA is designed by considering an electrically large cylindrical cavity with diameter $L = 30\lambda_0$. By initially assuming a completely reflecting PRS, the cavity height h is set to $h = \lambda_0/(2\sqrt{\varepsilon_r})$, according to (8) with $X_s = 0$. As previously discussed, the TRT can be applied to the TEN represented in figure 1 in order to obtain the relevant dispersion equation of the device. By numerically solving such expression for the complex improper roots, the dispersion curves for the leaky-wave phase and attenuation constants in the case of TE and TM modes are found [39]. Such a result is reported in figure 9, where the leaky-wave phase and attenuation constants are represented normalized with respect to the vacuum wavenumber k_0 for both the polarizations. In particular, the dispersion curves are reported for both TE and TM leaky modes over the frequency range 0.9–1.1 THz and for values of the chemical potential ranging from 0.3 eV to 1 eV.

As shown in figure 9, the TE and TM contributions (both in terms of β and α) are almost overlapped. This is due to the negligible differences of Z_s for the two polarizations and this implies almost the same behavior on both the principal planes in terms of radiation pattern, pointing angle, and beamwidth. The dispersion curves also show that the highest frequency that gives a broadside radiation is obtained for $\mu_c = 1$ eV. For this reason, the working frequency is fixed at the value for which the splitting condition [34], viz. $\beta = \alpha$, occurs for $\mu_c = 1$ eV, obtaining $f_{\tau=1\text{ps}} = 0.992$ THz and $f_{\tau=0.3\text{ps}} = 0.993$ THz, with obvious meaning of the subscripts. This frequency shift with respect to the theoretically expected $f_0 = 1$ THz is due to the nonzero value of the PRS sheet reactance X_s at 1 THz and $\mu_c = 1$ eV (see figure 8). Once the frequency is fixed, the performance of the FPC-LWAs can be theoretically predicted by using the values of β and α at the working frequency in the formulas introduced in section 2. At this point, the results obtained for a quasi-ideal and a realistic graphene model are reported in tables 1 and 2, respectively.

A high variability of the equivalent sheet reactance X_s and, in turn, of the leaky-mode dispersion curves with respect to the chemical potential μ_c is achieved at the working frequency, regardless the graphene-loss level (see figures 8 and 9). For this reason, a promising conical reconfigurable scanning range

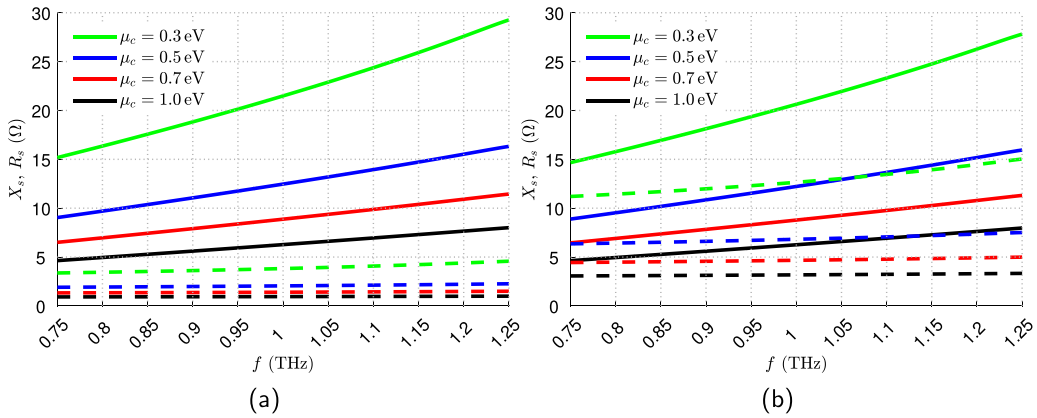

Figure 8. Equivalent reactance X_s (solid lines) and resistance R_s (dashed lines) for different chemical potentials μ_c vs. frequency f when a PRS unit cell with $p = \lambda_0/5$, $w = 0.1p$, and (a) $\tau = 1$ ps and (b) $\tau = 0.3$ ps is considered.

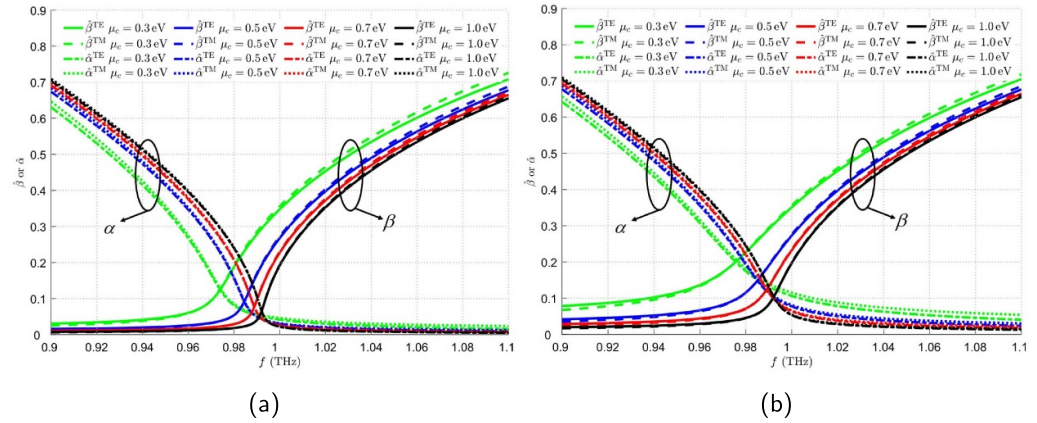

Figure 9. Dispersion curves of the normalized leaky-wave phase $\hat{\beta}$ and attenuation $\hat{\alpha}$ constants vs. frequency f when different chemical potentials μ_c are considered. The unit-cell configuration considered in this case has been implemented with $p = \lambda_0/5$, $w = 0.1\ p$, and relaxation time (a) $\tau = 1$ ps or (b) $\tau = 0.3$ ps.

(about 17°) is achieved for both a quasi-ideal and a realistic graphene model. The main differences between the two cases are given by the directivity D_0, the beamwidth $\Delta\theta$, and the radiation efficiency η_r, because they are strictly related to the leaky-wave attenuation constant (which is much higher in the lossy realistic graphene case). As expected, a lower-loss, narrower and more directive beam is achieved for quasi-ideal graphene rather than for the realistic case (see tables 1 and 2). However, also in the case of $\tau = 0.3$ ps, it is true that the radiation efficiency is low but it is still acceptable for a reconfigurable antenna in the THz frequency range with a sufficiently high directivity. It is worth pointing out that the D_0 values found through (9) and (10) are corroborated by the full-wave evaluations of the directivity D_0^{sim} reported in tables 1 and 2. In few cases, the theoretical directivity slightly overestimates the simulated one but this is due to the fact that the expression (10) should be considered quite accurate only for rather small beamwidths $\Delta\theta$.

In the evaluation of the antenna performance, also the radiation pattern computation plays an important role. Leaky-wave theory is able to analytically predict the radiated fields through cylindrical functions depending on β and α [28]. In figure 10, the theoretical results are clearly corroborated by the full-wave simulation of the entire 3D model of the device in terms of radiation pattern $P(\theta)$, normalized with respect to its maximum at the working frequency. Such results are shown on the H-plane, but very similar results are achieved on the E-plane

Table 1. Performance of the proposed antenna with $\tau = 1.0$ ps.

μ_c (eV)	θ_p	$\Delta\theta$	η_r (%)	D_0 (dB)	D_0^{sim} (dB)
1.0	0°	10.63°	8	25	25
0.7	7.09°	5.26°	11	22	21
0.5	10.94°	5.12°	15	21	19
0.3	17.23°	6.51°	25	18	17

Table 2. Performance of the proposed antenna with $\tau = 0.3$ ps.

μ_c (eV)	θ_p	$\Delta\theta$	η_r (%)	D_0 (dB)	D_0^{sim} (dB)
1.0	0°	16.91°	5	21	21
0.7	6.87°	11.54°	7	19	18
0.5	10.51°	12.39°	9	17	16
0.3	16.14°	15.94°	17	14	14

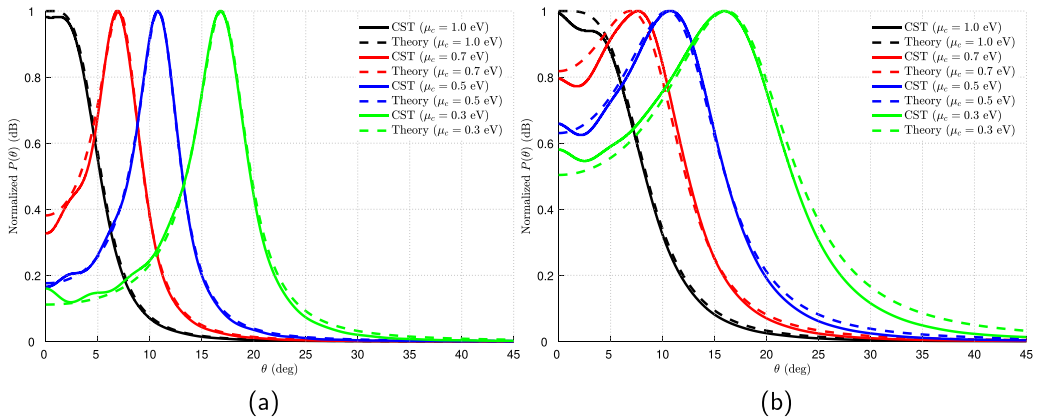

Figure 10. Comparison of far-field patterns on the H-plane at the working frequency achieved by a full-wave simulation of the entire structure (solid lines) and by the theoretical leaky-wave approach (dashed lines) when different μ_c are chosen. The unit-cell configuration considered in this case has been implemented with $p = \lambda_0/5$, $w = 0.1\ p$, and (a) $\tau = 1$ ps or (b) $\tau = 0.3$ ps.

thanks to the previously discussed properties of the proposed metasurface. It is worthwhile to point out that the impressive agreement in figure 10 clearly demonstrates that the far-field radiation pattern is mainly generated by the leaky-wave contribution, properly described by the proposed approach.

5. Conclusion

A Fabry–Perot cavity leaky-wave antenna based on an innovative hybrid metal–graphene metasurface has been proposed. Thanks to its configuration, by properly choosing the graphene portion of the unit cell, high reconfigurability properties and reduced ohmic losses with respect to previous graphene-based antennas can be achieved, even when graphene is modeled with values experimentally exhibited by state-of-the art samples. These results pave the way for the implementation of compact, planar, directive, and reconfigurable radiating devices working in the terahertz frequency range. The experimental validation of the proposed Fabry–Perot cavity leaky-wave antennas based on hybrid metal–graphene unit cell and the investigation of innovative metal–graphene metasurface designs will be the object of future works.

Data availability statement

No new data were created or analysed in this study.

Acknowledgments

E Negri, P Burghignoli, and A Galli acknowledge the partnership on “Telecommunications of the Future” (PE00000001 - program “RESTART”) supported by the European Union under the Italian National Recovery and Resilience Plan (NRRP) of NextGenerationEU. W Fuscaldo also acknowledges the project PRIN 2022 “SAFE” (Spiral and Focused Electromagnetic fields) 2022ESAC3K, Italian Ministry of University and Research (MUR), financed by the European Union, Next Generation EU.

ORCID iDs

Edoardo Negri https://orcid.org/0000-0001-8525-4306
Walter Fuscaldo https://orcid.org/0000-0002-0773-6286
Paolo Burghignoli https://orcid.org/0000-0001-5896-4732
Alessandro Galli https://orcid.org/0000-0002-5827-160X

References

[1] Leitenstorfer A *et al* 2023 *J. Phys. D: Appl. Phys.* **56** 223001
[2] Bauer M *et al* 2019 *IEEE Trans. Terahertz Sci. Technol.* **9** 430–44
[3] Heinz E, May T, Born D, Zieger G, Anders S, Zakosarenko V, Meyer H G and Schäffel C 2015 *J. Infrared Millim. Terahertz Waves* **36** 879–95
[4] Chen Z, Ma X, Zhang B, Zhang Y, Niu Z, Kuang N, Chen W, Li L and Li S 2019 *China Commun.* **16** 1–35
[5] Moradi K, Pourziad A and Nikmehr S 2021 *Optik* **228** 166201
[6] Zhang X, Cunjun R, Dai J, Ding Y, Ullah S and Kosar Fahad A 2021 *Int. J. Numer. Model.: Electron. Netw. Devices Fields* **34** e2911
[7] Esquius-Morote M Gomez-Diaz J S and Perruisseau-Carrier J 2014 *IEEE Trans. Terahertz Sci. Technol.* **4** 116–22
[8] Wang X C, Zhao W S, Hu J and Yin W Y 2015 *IEEE Trans. Nanotechnol.* **14** 62–69
[9] Fuscaldo W, Tofani S, Burghignoli P, Baccarelli P and Galli A 2018 Terahertz leaky-wave antennas based on metasurfaces and tunable materials *Metamaterials and Metasurfaces* (IntechOpen) pp 93–116
[10] Tofani S and Fuscaldo W 2020 *Condens. Matter* **5** 11
[11] Fuscaldo W, Tofani S, Zografopoulos D C, Baccarelli P, Burghignoli P, Beccherelli R and Galli A 2017 *IEEE Antennas Wirel. Propag. Lett.* **16** 2046–9
[12] Fuscaldo W, Burghignoli P, Baccarelli P and Galli A 2016 *IEEE Antennas Wirel. Propag. Lett* **15** 1545–8
[13] Fuscaldo W, Burghignoli P, Baccarelli P and Galli A 2017 *Int. J. Microw. Wirel. Technol.* **9** 1293—1303
[14] Zouaghi W, Voß D, Gorath M, Nicoloso N and Roskos H G 2015 *Carbon* **94** 301–8
[15] D’Arco A, Mussi V, Petrov S, Tofani S, Petrarca M, Beccherelli R, Dimitrov D, Marinova V, Lupi S and Zografopoulos D C 2020 *Nanotechnology* **31** 364006
[16] Fuscaldo W, De Simone S, Dimitrov D, Marinova V, Mussi V, Beccherelli R and Zografopoulos D C 2022 *J. Phys. D: Appl. Phys.* **55** 365101

[17] Burghignoli P, Fuscaldo W and Galli A 2021 *IEEE Antennas Propag. Mag.* **63** 116–45
[18] Wang D W *et al* 2017 *IEEE Trans. Nanotechnol.* **16** 1132–7
[19] Hosseininejad S E and Komjani N 2016 *IEEE Trans. Antennas Propag.* **64** 3787–93
[20] Jin J, Cheng Z, Chen J, Zhou T, Wu C and Xu C 2020 *Int. J. RF Microw. Comput.-Aided Eng.* **30** e22175
[21] Fuscaldo W, Torabi E, Zografopoulos D C, Erricolo D and Beccherelli R 2023 *IEEE Access* **11** 91831–41
[22] 2021 CST products Dassault Systèmes France (available at: www.cst.com)
[23] Hanson G W 2008 *IEEE Trans. Antennas Propag.* **56** 747–57
[24] Banszerus L, Schmitz M, Engels S, Dauber J, Oellers M, Haupt F, Watanabe K, Taniguchi T, Beschoten B and Stampfer C 2015 *Sci. Adv.* **1** e1500222
[25] Fuscaldo W, Burghignoli P, Baccarelli P and Galli A 2017 *IEEE Trans. Antennas Propag.* **65** 1651–60
[26] Galli A, Baccarelli P and Burghignoli P 2016 *Wiley Encyclopedia of Electrical and Electronics Engineering* ed J G Webster (Wiley) pp 1–20
[27] Negri E, Fuscaldo W, Tofani S, Burghignoli P and Galli A 2024 *Sci. Rep.* **14** 3892
[28] Ip A and Jackson D R 1990 *IEEE Trans. Antennas Propag.* **38** 482–8
[29] Negri E, Fuscaldo W, Burghignoli P and Galli A 2023 *IEEE Trans. Antennas Propag.* **71** 1424–36
[30] Jackson D R, Burghignoli P, Lovat G, Capolino F, Chen J, Wilton D R and Oliner A A 2011 *Proc. IEEE* **99** 1780–805
[31] Fuscaldo W 2020 *IEEE Trans. Antennas Propag.* **68** 643–55
[32] Sorrentino R and Mongiardo M 2005 *Transverse Resonance Techniques* (Wiley, Ltd)
[33] Tretyakov S 2003 *Analytical Modeling in Applied Electromagnetics* (Artech House)
[34] Lovat G, Burghignoli P and Jackson D R 2006 *IEEE Trans. Antennas Propag.* **54** 1442–52
[35] Fuscaldo W, Galli A and Jackson D R 2022 *IEEE Trans. Antennas Propag.* **70** 7853–68
[36] George P A, Hui W, Rana F, Hawkins B G, Smith A E and Kirby B J 2008 *Opt. Express* **16** 1577–82
[37] Balanis C A 2016 *Antenna Theory: Analysis and Design* (Wiley)
[38] Fuscaldo W, Tofani S, Zografopoulos D C, Baccarelli P, Burghignoli P, Beccherelli R and Galli A 2018 *IEEE Trans. Antennas Propag.* **66** 1169–78
[39] Galdi V and Pinto I M 2000 *Microw. Opt. Technol. Lett.* **24** 135–40